

Contents lists available at ScienceDirect

## Journal of Volcanology and Geothermal Research

journal homepage: www.journals.elsevier.com/journal-of-volcanology-and-geothermal-research





# Determining the umbrella cloud geometry of unwitnessed silicic explosive eruptions: A case study from Mount Mazama (Oregon, United States)

Joshua Wiejaczka\*, Thomas Giachetti

University of Oregon, Department of Earth Sciences, Eugene, OR, United States

#### ARTICLE INFO

Keywords:
Tephra dispersal
Grain-size distribution
Eruption source parameters
Umbrella cloud
Explosive volcanism

#### ABSTRACT

Volcanic Ash Transport and Dispersal Models (VATDMs) make real-time forecasts of tephra fall resulting from explosive eruptions possible. However, these predictions still mainly rely on eruption source parameters, such as erupted mass, total grain-size distribution, and plume height, gathered via thorough studies of past eruptions similar in nature. This dependency of eruption source parameters to analogous eruptions becomes particularly challenging when there are limited instances of similar events. An example is rhyodacitic to rhyolitic eruptions. This type of volcanic eruption has only been witnessed twice, at Chaitén (2008-2009) and Cordón Caulle (2011-2012), both in Chile. Here, we examine the 7.7 ka Cleetwood eruption of Mount Mazama (Oregon, USA), as a case study. This rhyodacitic eruption started explosively with two initial VEI 4, subplinian phases, and ended effusively with the emplacement of a rhyodacitic flow. We use the results of a detailed study of the proximal and medial tephra deposits as input in a VATDM to investigate the geometry and dimensions of the main plume formed during the Cleetwood eruption. We 1) constrain the erupted mass and calculate a detailed total grain-size distribution, 2) explore the Reanalysis 2 wind database to determine the direction and velocity of the local wind at the time of the eruption, and 3) use the VATDM Tephra2 with a grid-search method to estimate plume height, mass distribution within the plume, and the characteristics of tephra diffusion. We find that a vertical release of the erupted mass along a single line above the vent adequately replicates the measured mass loads but fails to simultaneously fit measured grain-size distributions at the same locations. We thus devise a method that not only accounts for a customized total grain-size distribution, real 1D wind patterns, and variable mass distribution within the plume, but also allows for adjustments to the size and location of an elliptical umbrella cloud. Using this method, we successfully replicate both local mass loads and high-resolution grain-size distributions and show that particles  $\geq$ 0.125 mm from the lower Cleetwood unit were likely deposited from a 5  $\times$  45 km<sup>2</sup> umbrella reaching 16 km a.s.l., elongated in the direction of main wind intensity. This research contributes to enhancing the accuracy of predicting tephra transport from silicic volcanic eruptions. Moreover, it underscores the importance of utilizing grain-size data in combination with mass loads at specific locations to gain insights into the characteristics of the eruption plume, especially for eruptions that have not been directly observed.

## 1. Introduction

Tephra fallout during volcanic eruptions presents a wide range of hazards that can have significant impacts on human health, infrastructure, and the environment. The physical hazards of tephra fallout include the potential for injury or fatality; larger tephra fragments can cause blunt trauma, while smaller particles can lead to eye and respiratory irritation by penetrating deep into the respiratory system, exacerbating preexisting conditions, and/or causing new respiratory distress (Baxter, 2005). Tephra accumulation poses risks to infrastructure,

including collapse of roofs and structures under the weight of volcanic ash, which is compounded when wet (Blong, 1984). Likewise, the agricultural sector is vulnerable to tephra fallout, as the latter can damage crops, contaminate water sources, and hinder photosynthesis by blocking sunlight (Wilson et al., 2012). This highlights the importance of the accuracy of Volcanic Ash Transport and Dispersal Models (VATDMs) used for real-time forecasting and probabilistic hazard assessments of tephra fallout.

VATDMs use either a Lagrangian particle tracking numerical approach (e.g., Puff; Searcy et al., 1998; HYSPLIT, Draxler and Hess,

E-mail address: jwiejacz@uoregon.edu (J. Wiejaczka).

<sup>\*</sup> Corresponding author.

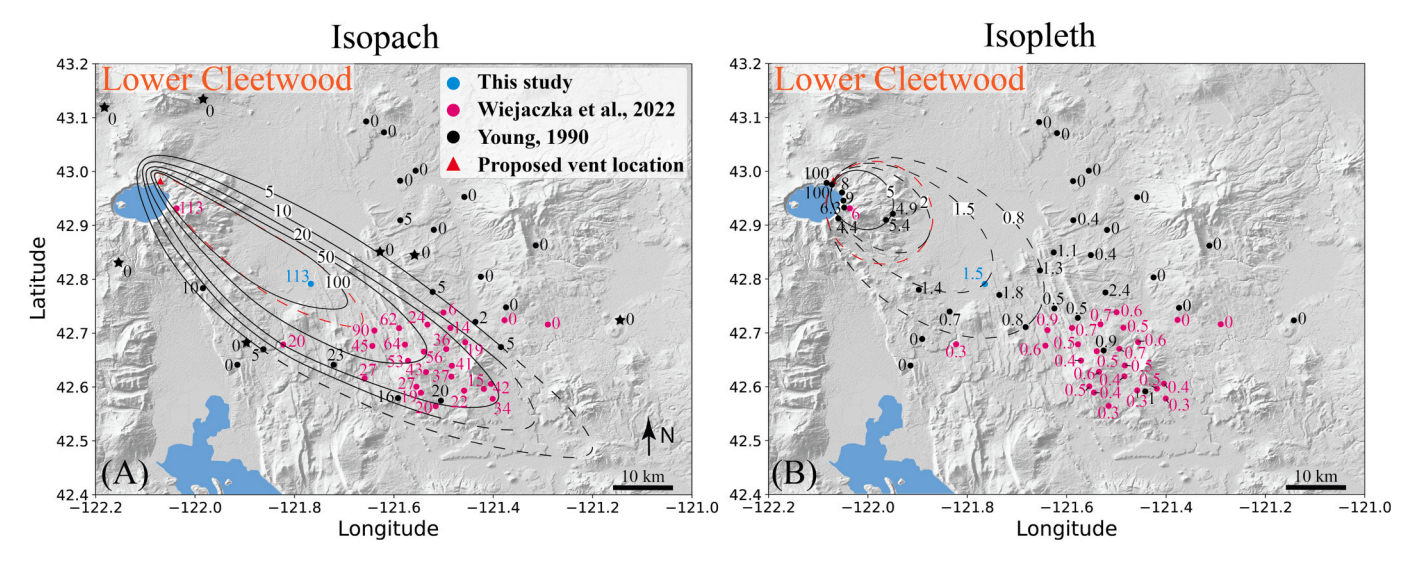


Fig. 1. (A) Isopach and (B) maximum lithic (ML) isopleth maps for the lower Cleetwood unit. All isolines are in centimeters and dashed red isolines represent the original lines from Wiejaczka and Giachetti, 2022. Black stars on the isopach map denote zero thickness boundary points from Young (1990) used in modeling. Background is global earth relief (Tozer et al., 2019). (For interpretation of the references to colour in this figure legend, the reader is referred to the web version of this article.)

1998), a Eulerian advection-diffusion numerical approach (e.g., Ash3d, Schwaiger et al., 2012; NAME, Jones et al., 2007; Fall3D, Folch et al., 2020), or a Eulerian advection-diffusion analytical approach (e.g., Tephra2, Bonadonna et al., 2005; Connor and Connor, 2006; Volentik et al., 2009; Biass et al., 2016). While these models consider different secondary variables such as topography, particle shape, wet/dry particle aggregation, and have diverse options for how the erupted mass is initially distributed in the atmosphere (i.e., point source, line source, umbrella cloud, etc.), all rely on detailed field studies of analogous eruptions to provide constraints on both the primary input Eruption Source Parameters (ESPs) and the output of the model. ESPs include the erupted mass (M), plume height (Ht), and the Total Grain-Size Distribution (TGSD) of particles ejected into the atmosphere. The TGSD, which is crucial for accurate forecasts, is particularly difficult to constrain. It affects the distribution of particles within the plume and, in turn, modulates the location and timing of when a particle will be deposited. In situ measurements of TGSD during an eruption prove difficult (Scollo et al., 2005; Gouhier and Donnadieu, 2008; Bonadonna et al., 2011; Kozono et al., 2019; Freret-Lorgeril et al., 2019), especially for high-flux, large plume eruptions. Moreover, constructing a TGSD from historic events is often complicated due to poor deposit exposure and preservation, especially very close and very far from the vent (Costa et al., 2016; Pioli et al., 2019).

The dependence of VATDMs on ESPs from analogous historic eruptions becomes more problematic when, for a given type of ongoing eruption, the catalog of similar, historically observed events is limited. An example is that of silicic eruptions that transition from explosive to effusive activity. Although many of these deposits have been identified in the historic record (e.g., the 1060 CE Glass Mountain eruption of Medicine Lake volcano; Heiken, 1978; or the 700 CE Big Obsidian Flow eruption at Newberry Volcano; Kuehn, 2002; Trafton and Giachetti, 2022), the only direct observations of this behavior are from recent eruptions at two Chilean volcanoes; Chaitén in 2008 (Castro and Dingwell, 2009) and Cordón Caulle in 2011-2012 (Pistolesi et al., 2015; Schipper et al., 2013). The ~7.7 ka Cleetwood eruption of Mount Mazama (Crater Lake/giiwas, Oregon, USA) appears to also be one such silicic eruption that transitioned from explosive to effusive activity (Young 1990). The Cleetwood eruptive sequence consisted of two consecutive VEI 4 eruptions, the lower and upper Cleetwood units. The lower Cleetwood unit is the first and main phase, with a tephra deposit volume close to 1 km<sup>3</sup> (Wiejaczka and Giachetti, 2022). Following the upper Cleetwood phase ( $\sim$ 0.2 km³), the eruptive activity transitioned to an effusive stage, producing a rhyodacitic flow with a minimum volume of  $\sim$ 0.6 km³ (Bacon, 1983). This eruption was soon followed by the climactic caldera-forming eruption that created Crater Lake, which was one of the largest of the Holocene Epoch (60 km³ DRE; Bacon, 1983; Buckland et al., 2021), pointing towards the Cleetwood eruptive sequence as potentially key in destabilizing a much larger magmatic system.

In this study, we first re-evaluate the field-derived ESPs (M, H<sub>b</sub> and TGSD) for the lower Cleetwood by adding new field data to those of Young (1990) and Wiejaczka and Giachetti (2022). Next, we use these field-derived ESPs, a large collection of reconstructed wind profiles, and a grid search approach using Tephra2 to explore the geometry of the lower Cleetwood plume and the diffusion characteristics of the tephra, by minimizing the misfits between the model output and both mass loads and grain-size distributions obtained in the field. We demonstrate that comparing high-resolution grain-size distributions from individual locations with model outputs has the potential to give insight into the plume geometry for unwitnessed historic eruptions.

#### 2. Methods

## 2.1. Field

The samples used in this study are those collected by Wiejaczka and Giachetti (2022). An additional pit was dug in 2022 (42.792344, -121.765731) approximately 32.5 km southeast from the supposed vent, on the main dispersal axis of the lower Cleetwood tephra fall deposit (Fig. 1). At this location, below 3.4 m of tephra from the climactic phase of the Mazama eruption, the Cleetwood deposit was divided into the lower and upper Cleetwood units based on changes in grain-size and grading. Each unit was then measured, photographed, and several kilograms of each unit were collected for analysis. Before analysis, samples were dried over night at 80  $^{\circ}\mathrm{C}$  to remove adsorbed water.

## 2.2. Deposit density and mass load

Deposit density for each location was calculated by pouring bulk samples into a graduated cylinder and measuring both the mass and volume of the sample. Where samples were divided into subunits, the thickness fraction of each subunit was used as a weight to calculate the

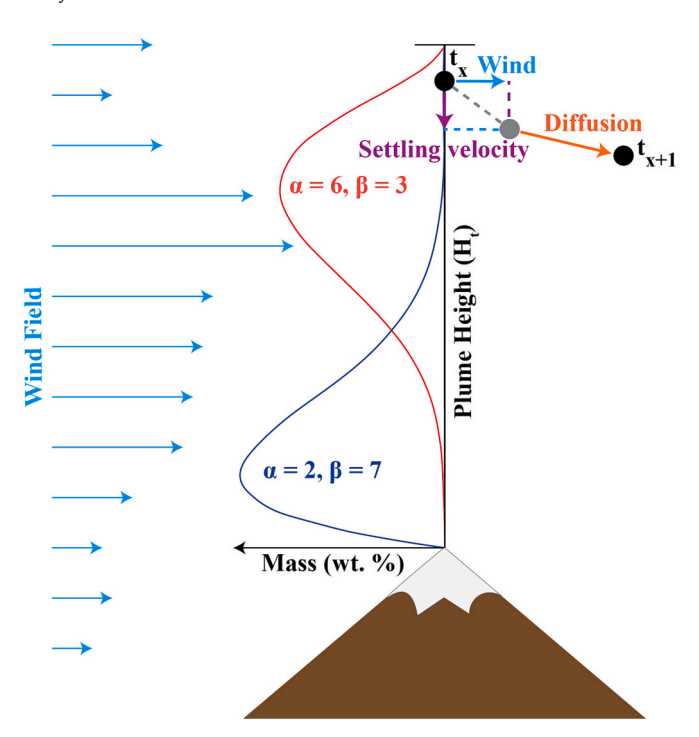


Fig. 2. Schematic showing how Tephra2 operates. Particles are first released instantaneously along a single vertical line located directly above the vent and begin to fall through a layered atmosphere. Each particle's trajectory is then modified by the wind velocity and heading of each layer, and further by atmospheric diffusion. Particles are distributed within the plume using the equation  $P(H_t) = \frac{(1-H_t)^{\beta-1}H_t^{\alpha-1}}{B(\alpha,\beta)}$  where  $H_t$  is plume height and  $B(\alpha,\beta)$  is the beta function. Changing  $\alpha$  and  $\beta$  in the beta function modifies the way in which mass is initially distributed along the vertical line (i.e., the plume).

whole lower Cleetwood deposit density at that location. The mass load for each location was then calculated by multiplying its thickness measured in the field by the deposit density measured in the lab. The mass load of the whole deposit was obtained by multiplying the average density of all twenty-five locations by the deposit volume (see Section 2.3 for volume calculation).

## 2.3. Erupted volume

The isopach map of the lower Cleetwood (Fig. 4A in Wiejaczka and Giachetti, 2022) was updated by redrawing the 100 cm isoline using Adobe Illustrator. It is the only isoline that required modification following the addition of the new sample location described above (Fig. 1A). The area enclosed within individual isolines was calculated using the image processing package Fiji (ImageJ; Schindelin et al., 2012). The lower Cleetwood tephra fall volume was then re-calculated with the probabilistic mode in *TephraFits* (Biass et al., 2019) using the exponential, power-law, and Weibull models and the erupted mass (M) was then determined by multiplying the volume by the average deposit density.

## 2.4. Plume height

The maximum lithic value for the newly added location (Cltwd 2) was calculated using digital calipers in the lab and averaging the diameters of the five largest lithics. The isopleth map of the lower Cleetwood (Fig. 4C in Wiejaczka and Giachetti, 2022) was updated by slightly altering the 2 cm maximum lithic isoline and adding a 1.5 cm lithic isoline using Adobe Illustrator to include the additional data point (Fig. 1B). Downwind and crosswind distances, as well as isopleth areas, were calculated using Fiji and the plume height,  $H_t$  (km) was then re-

estimated using the models of Carey and Sparks (1986), Bonadonna and Costa (2013), and Rossi et al. (2019), herein referred to as CS86, BC2013, and R2019, respectively.

#### 2.5. High-resolution grain-size distributions

#### 2.5.1. Individual distributions

Individual high-resolution grain-size distributions (HR-GSDs) were determined following the sample preparation and methodology detailed in Wiejaczka and Giachetti (2022). The reader is referred to this paper for a full description of the methods used, only a summary being given here. After being dried, all samples were dry-sieved every phi size from 5 to −6 (i.e., 0.031 mm to 64 mm). The volume and equivalent diameter of particles ≥0.125 mm of all samples were then determined via dynamic image analysis (DIA) with a Microtrac PARTAN 3D particle size analyzer at the University of Oregon (Trafton and Giachetti, 2021; Wiejaczka and Giachetti, 2022). The volume of each particle is determined by multiplying its average length, width, and thickness and an equivalent diameter is calculated assuming a sphere of equal volume. Volume distribution of particles <0.125 mm was obtained for each size fraction by laser diffraction on a Beckman Coulter LS 13320 (Fig. 2E; Blott and Pye, 2006; see also Wiejaczka and Giachetti, 2022).

Results of grain size analyses from both DIA and laser methods were then sorted in fifty regularly-spaced logarithmic bins from 12 to -7 phi (i.e., 0.2 µm - 128 mm). Laser diffraction data being given in volume percent as a function of equivalent diameter, each size fraction < 0.125 mm was first converted to an actual volume using the mass of the size fraction (measured after sieving on a high-precision balance) and its bulk density measured using a Micromeritics AccuPyc II 1340 helium pycnometer, assuming porosity in particles <0.125 mm is negligible. The two datasets were then merged to produce a continuous HR-GSD: we used laser diffraction data for size fractions < 0.125 mm, and DIA data for size fractions >0.125 mm. For locations where the lower Cleetwood deposit was divided into subunits, a HR-GSD was produced for each sub-unit and the HR-GSD of the whole lower Cleetwood was obtained by averaging the sub-units HR-GSDs, using the relative thicknesses of the sub-units as weights. Note that the grain size distribution below 0.125 mm was measured by laser diffraction for half of the samples only. For the other half, a 'high-resolution' grain size distribution below 0.125 mm was interpolated from the sieve data of size fractions 0-0.032 mm, 0.032-0.063 mm, and 0.063-0.125 mm. This procedure, which greatly accelerates sample analysis, does not affect the results because 1) the <0.125 mm fraction represents only <4.2 wt% of each of these samples (except for Cltwd36 for which it accounts for 10.2% of the sample mass), and 2) this study focuses on transport of lapilli and ash coarser than 0.125 mm.

#### 2.5.2. Total grain-size distribution

To create a high-resolution Total Grain-Size Distribution (HR-TGSD, i.e., of the whole deposit, not just a single location) to use as an input in Tephra2 and to compare model output to field-based HR-GSDs, our volume distributions first need to be converted into mass distributions. This was done for each individual HR-GSD following the density model of Bonadonna and Phillips (2003). Their model assumes a constant density for both a smaller and larger particle boundary, with a linear increase in density between these two set bounds. We use 2380 kg/m<sup>3</sup> for all particles < 0.063 mm and  $481 \text{ kg/m}^3$  for all particles > 2 mm. The lower bound is the density of the glass determined by helium pycnometry by Wiejaczka and Giachetti (2022), and the upper bound was calculated by averaging the mass of all measured particles >2 mm divided by their volume determined via DIA. Following Wiejaczka and Giachetti (2022), the HR-TGSD was then calculated by applying the Voronoi tessellation method (Bonadonna and Houghton, 2005) using the twenty-five HR-GSDs. This method creates Voronoi polygons of the area of interest in which all points inside a polygon are best represented by a central sample point, or centroid. The HR-TGSD is calculated by

multiplying the HR-GSD of the centroid by the mass fraction of its representative Voronoi polygon, and then summing all weighted HR-GSDs.

#### 2.6. Wind

Wind direction and velocity profiles at the supposed location of the Cleetwood vent (42.982275, -122.069576; Wiejaczka and Giachetti, 2022) were retrieved using the NCEP-DOE Reanalysis 2 database (Kanamitsu et al., 2002). All data available were gathered, that is four times daily (at 00:00, 06:00, 12:00, 18:00 UTC) over the timeframe of 1979–2022, corresponding to the first to latest wind field available at the time of writing, and totaling 64,284 wind fields. Wind files were then filtered to find and use only those for which the average wind direction between altitudes of 2 km (vent elevation) and 21 km (i.e., for a 19-kmhigh plume as determined by Wiejaczka and Giachetti, 2022) falls within 2° of the main dispersal axis of the lower Cleetwood unit (i.e., N129°  $\pm$  2°).

## 2.7. Tephra2

For a complete description of the model, list of equations, and different versions of the Tephra2 VATDM, the reader is referred to Bonadonna et al. (2005, 2012), Connor and Connor (2006), Volentik et al. (2009, 2010), Biass et al. (2016), Constantinescu et al. (2021), and references therein, only the main points pertaining to this study being discussed here. We have chosen to use Tephra2 because, as explained below, it solves the advection-diffusion equation analytically (Bonadonna et al., 2005), instead of numerically, leading to much faster runtimes ( $\sim$ 0.1–1 s per run on a single processor laptop) and allowing for a broader exploration of plume and tephra diffusion characteristics. The fact that this model does not account for particle aggregation does not impact our results as this study focusses on the transport of particles  $\leq$ 3  $\varphi$  (i.e.,  $\geq$  0.125 mm) where aggregation is believed to have a minimal impact on sedimentation (Rose and Durant, 2011; Brown et al., 2012). The use of this model in the context of this study is also justified as the area of interest is within 100 km of the vent location (Biass et al., 2016).

The Tephra2 VATDM solves the advection–diffusion equation analytically to determine the final mass per unit area (i.e., mass load, in  $kg/m^2$ ) and relative grain-size distribution (in wt%) of a tephra fall on the ground at points (x, y) within a 2D modeled space. Particles are released instantaneously from a plume located directly above the vent and fall through a layered atmosphere. A particle's trajectory is modified by the wind velocity of each layer, and further by atmospheric turbulent diffusion (Fig. 2). Particles are assumed to be spherical and have a size-dependent density. Their settling velocity is determined by their Reynolds number (see details in Bonadonna et al., 1998).

Tephra2 requires the user to provide 1) the eruption source parameters, 2) a density versus size model, and 3) a 1D wind field in which both speed and direction vary with elevation. Tephra2 does not account for horizontal and temporal heterogeneities in the wind. The ESPs include plume height (H<sub>I</sub>), erupted mass (M), and the total grain-size distribution (TGSD). Here we use TephraProb, the modified version of Tephra2 of Biass et al. (2016), which allows the user to provide a custom TGSD, as opposed to a Gaussian TGSD based on median grain-size and standard deviation. The user also provides parameters that control the initial vertical mass distribution within the plume via a beta function with variables  $\alpha$  and  $\beta$ . When  $\alpha<\beta$ , mass is shifted towards the base of the plume, whereas the opposite occurs when  $\alpha>\beta$ . If  $\alpha=\beta=1$ , the beta function becomes linear, and mass is distributed equally along the vertical axis. Both  $\alpha$  and  $\beta$  are greater than zero, with values presented in the literature never exceeding 10 (Bonadonna et al., 2010; Elissondo et al., 2016).

Finally, a user-input atmospheric turbulent diffusion coefficient (DC, in  $m^2/s$ ) and fall time threshold (FTT, in s) are used to control how particles diffuse in the atmosphere. In the model, particle diffusion is

size dependent and governed by a linear diffusion until the time exceeds FTT, at which point a power law diffusion is used (Bonadonna et al., 2005; Suzuki, 1983). The latter is partly controlled by the eddy diffusivity constant (0.04 m²/s; Suzuki, 1983). Values presented in the literature for DC and FTT cover orders of magnitude, ranging from  $\sim\!10^2\!-\!10^5$  m²/s and  $\sim\!10^2\!-\!10^4$  s, respectively (e.g., Bonadonna et al., 2010; Volentik et al., 2010; Johnston et al., 2012; Biass et al., 2016). If the ESPs and the density model are usually derived from field data, values for  $\alpha$ ,  $\beta$ , DC, and FTT are typically determined via inversion.

## 2.8. Tephra2 grid search

Using the filtered wind files, we conducted a grid search in parameter space using Tephra2 to estimate the combination of plume height ( $H_t$ ), erupted mass (M), alpha  $(\alpha)$ , beta  $(\beta)$ , diffusion coefficient (DC) and fall time threshold (FTT) that give the best fit of the model to the data. To do so, the TGSD derived from the field was kept constant, whereas  $H_t$ , M,  $\alpha$ ,  $\beta$ , DC, and FTT were all varied. The parameters  $\alpha$  and  $\beta$  were each explored over the range 1–10, plume height between 9 and 30 km, mass within (3.3–9.0)  $\times$   $10^{11}$  kg and both the diffusion coefficient (m²/s) and the fall time threshold (s) were varied over  $10^2-10^6$ . For each run, the Root-Mean-Square Error, RMSE, of the mass load and GSDs were determined by

$$RMSE = \sqrt{\sum_{i=1}^{n} \frac{(y_i - \hat{y}_i)^2}{n}}$$
 (1)

Where  $y_i$  is the observed result;  $\widehat{y}_i$  is the modeled result, and n is the number of locations or grain-size bins. For mass load, the RMSE ('RMSE ML') is a single value and n is equal to the 37 sample locations (one mass load per location). To further constrain the edges of the modeled space we have included the locations of zero thickness from Young (1990) which are closest to our isopach when no data from our field campaigns are present (black stars in Fig. 1A). For the RMSE of the grain size distribution ('RMSE GSD'), n is equal to the 27 size bins  $\leq 3$   $\phi$  ( $\geq 0.125$  mm) and one RMSE GSD is calculated for each of the 25 locations for which a sample was collected and a GSD produced. To obtain a single RMSE GSD value for each model run and estimate the overall goodness of the fit of that run to the grain size distributions data, the median of these 25 values was used. This study solely focuses on particles  $\leq 3$   $\phi$  ( $\geq 0.125$  mm) in the proximal and medial deposit, which accounts for  $\sim 96$  wt% of the modeled mass.

#### 3. Results

#### 3.1. Field

The additional pit dug in 2022 (Cltwd 2) lies on the main dispersal axis of the lower Cleetwood tephra fall deposit, approximately 32.5 km from the proposed vent. At this location, the Cleetwood deposit overlies the Llao Rock tephra fall (47 cm) and is covered first by 2.5 cm of the Basal Ash and then by 340 cm of the lower and upper pumice units of the Climactic eruption (Young, 1990; Supplementary Fig. 1). The two units of the Cleetwood eruption, lower and upper, are present at this location. The lower Cleetwood is 113 cm thick and exhibits strong normal grading. The base of this phase makes sharp contact with the top of the Llao Rock deposit, which shows signs of reworking. Median clasts are 19.0 mm at the base of the lower Cleetwood deposit, grading into smaller grains with a median of 5.4 mm at the top. Interestingly, ~8 cm above the contact between Llao Rock and the lower Cleetwood, pumices are coated in what was identified as charcoal. This band of charcoalcoated pumice is ~10 cm thick and pumices return to a white-grey color for the remainder of the lower Cleetwood deposit. The upper Cleetwood unit at this location is 3.5 cm thick and reversely grades into the overlying Basal Ash unit of the Climactic eruption (Young, 1990).

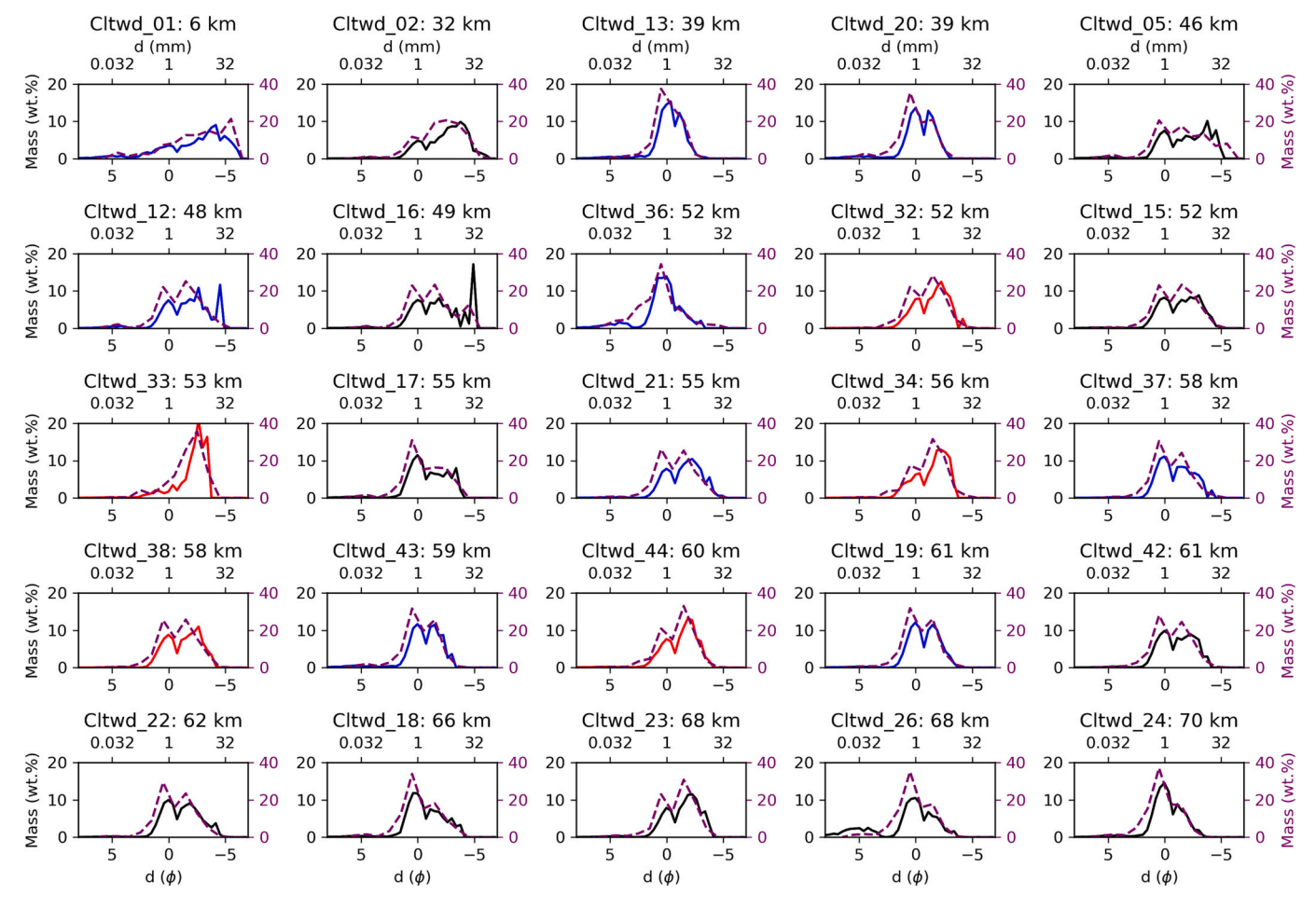


Fig. 3. Individual Grain-Size Distributions of the lower Cleetwood unit for 25 locations ranging from 6 to 70 km from the proposed vent location. High-Resolution Grain-Size Distributions (HR-GSDs) are represented by solid lines. Colour shows the relative locations compared to the main dispersal axis: black is  $129^{\circ} \pm 2^{\circ}$  from North (i.e., along the main dispersal axis), red is north of this line, and locations south of this line are shown in blue. The dashed purple line is the low-resolution GSD obtained from sieving. Note that the left and right y-axes have different scales. (For interpretation of the references to colour in this figure legend, the reader is referred to the web version of this article.)

## 3.2. Deposit density and mass load

Deposit densities and mass loads for all locations can be found in Supplementary Table 1. Deposit densities range from  $438\pm7~kg/m^3$  to  $772\pm4~kg/m^3$ , with an average value of  $526\pm86~kg/m^3$ . Most locations having a deposit density in the range  $450–550~kg/m^3$ . The location closest to the vent, Cltwd 1, has a large deposit density of  $768\pm5~kg/m^3$  because of the presence of large lithic clasts. Mass loads vary between  $26\pm3~kg/m^2$  and  $867\pm9~kg/m^2$  and generally decrease with increasing distance from the vent, as expected.

## 3.3. Erupted volume and mass

The isopach map of the lower Cleetwood was redrawn following the addition of location Cltwd 2, further constraining the 100 cm isoline. The erupted volume was then recalculated using the probabilistic mode (n = 100,000) of TephraFits (Biass et al., 2019) (Fig. 1A; Supplementary Table 2) for the exponential, power-law, and Weibull models, giving (non-DRE) deposit volume ranges of 0.76–1.02 km³, 1.30–1.47 km³, and 0.80–0.98 km³, respectively (Supplementary Table 2). Using the full range of calculated erupted volumes, along with the average deposit density of all 25 locations (526  $\pm$  86 kg/m³, see above), gives a range for the erupted mass, M, equal to (3.3–9.0)  $\times$   $10^{11}$  kg.

## 3.4. Plume height

New maximum lithic data from Cltwd 2 made it possible to add a 1.5 cm isopleth isoline to those drawn by Wiejaczka and Giachetti (2022), and to further constrain the 2 cm isoline (Fig. 1B). Recalculating the plume height (H<sub>t</sub>) of the lower Cleetwood unit (Supplementary Table 3) using the CS86 model gives a  $H_t$  of 24.4  $\pm$  2.2 km, with a windspeed of  $35 \pm 8$  m/s (as a comparison, Wiejaczka and Giachetti, 2022, obtained  $23.5 \pm 2.3$  km and 24 m/s wind speed). As shown in Fig. 3 of the supplementary material of Wiejaczka and Giachetti (2022) and in Section 1.6. of this study, such strong winds (>30 m/s) are common above Crater Lake, especially between 5 and 15 km a.s.l. Using eq. 7 from Bonadonna and Costa (2013) and a  $\lambda$  value of 7.4 from best fitting the square root of isopleth areas from Fig. 1B to the Weibull equation, gives a  $H_t$  value of 15.1 km. The R2019 model fails for the isoline of 0.8 cm and gives a total range of 14.4  $\pm$  4.4 km when considering eruptive scenarios 2 (intermediate intensity) and 3 (high intensity; see Rossi et al., 2019) for the 5, 2, and 1.5 cm maximum lithic isolines altogether. This value is lower than the 18.9  $\pm$  1.7 km obtained by Wiejaczka and Giachetti (2022) using the same model. Considering all three models gives a wide range of possible plume heights between 9.0 and 27.3 km.

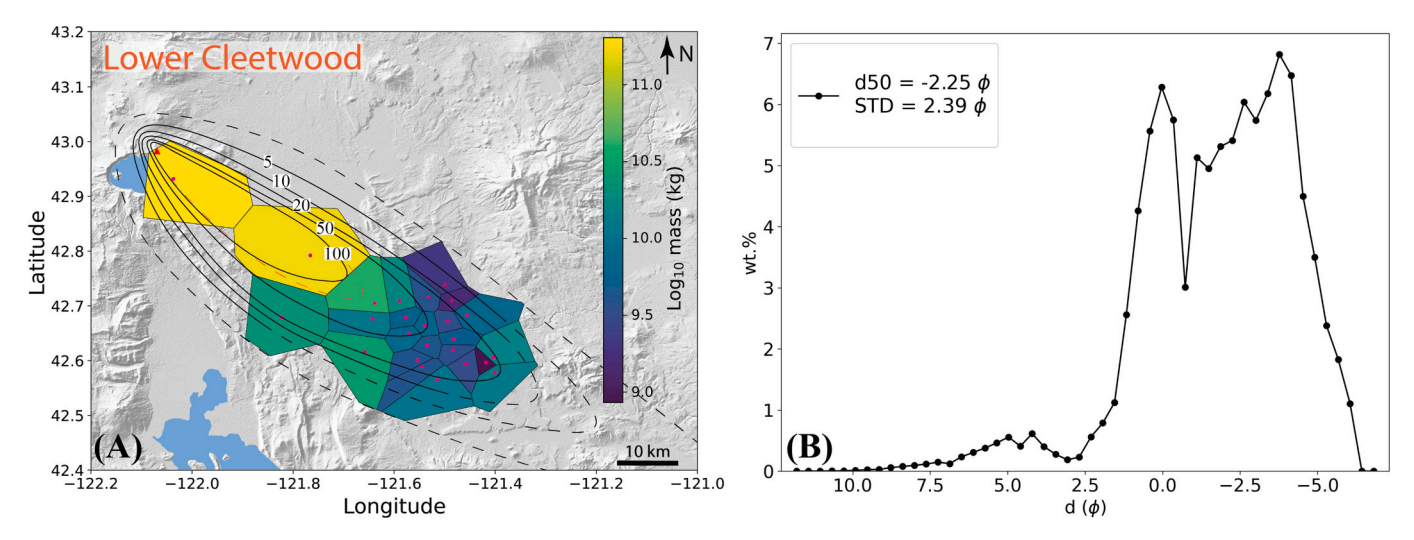


Fig. 4. (A) Voronoi tessellation of the lower Cleetwood unit. Isolines are in centimeters and the dashed red line is the 100-cm isoline from Wiejaczka and Giachetti (2022). Background is global earth relief (Tozer et al., 2019). (B) Total grain-size distribution of the lower Cleetwood unit obtained using Voronoi tessellation, with a median grain-size of  $-2.25 \, \varphi$  (4.76 mm) and a standard deviation of 2.39  $\varphi$  (0.19 mm). (For interpretation of the references to colour in this figure legend, the reader is referred to the web version of this article.)

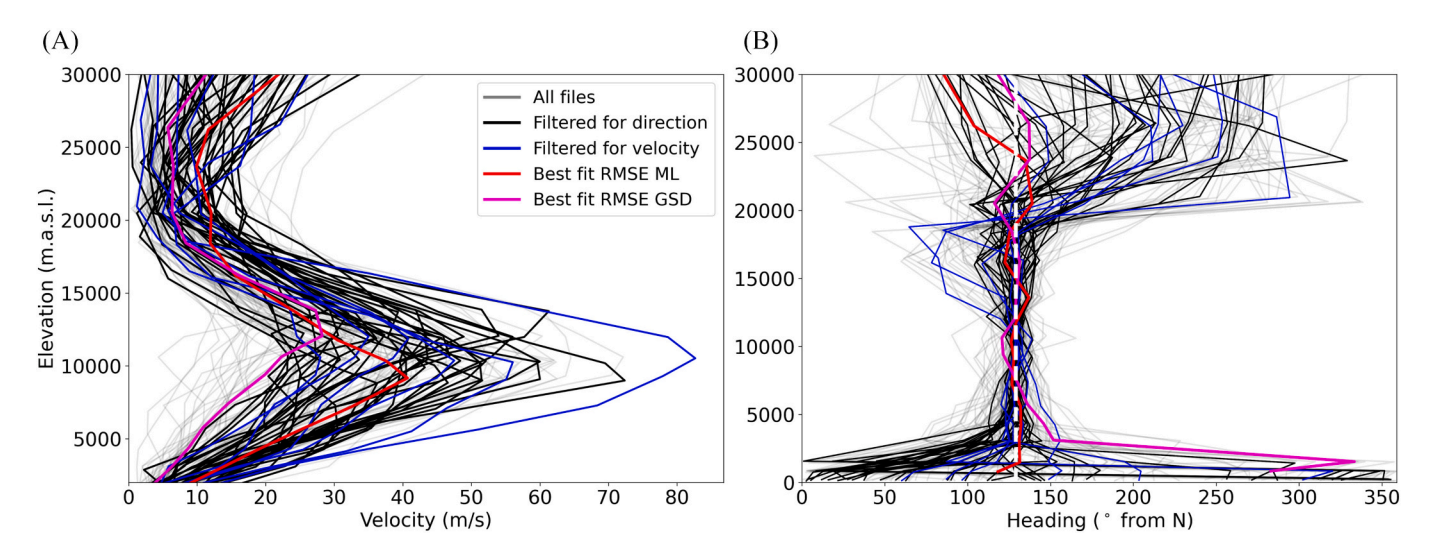


Fig. 5. (A) Wind velocity profile in m/s. Elevation is in meters above sea level (m.a.s.l.). Profile is calculated for inferred location of the Cleetwood vent, at 42.982275, -122.069576 (Wiejaczka and Giachetti (2022)). (B) Wind heading (° from North) as a function of elevation. White dashed line represents the main dispersal axis (129° from North), inferred from the deposit.

## 3.5. High-resolution grain-size distributions

#### 3.5.1. Individual grain-size distributions

Individual HD-GSDs were calculated for the 25 locations in Wiejaczka and Giachetti (2022) and this study (Fig. 3). GSDs for all locations are rather coarse with ~96% of the mass being  $\leq 3 \varphi$  ( $\geq 0.125$  mm). Each GSD exhibits at least two modes, and some locations (e.g., Cltwd 26 and Cltwd 36) show three modes. For 84% of the GSDs, the two major modes occur at  $-0.88 \varphi < d \leq 3 \varphi$  ( $0.125 \text{ mm} \leq d < 1.8 \text{ mm}$ ) and  $\leq -0.88 \varphi$  ( $d \geq 1.8 \text{ mm}$ ), whereas the third mode, when present, is around  $5 \varphi$  (0.032 mm). Note that this bimodality is not an artifact of converting DIA volume to mass as it is observed in the GSD obtained using lower resolution sieve data (see purple dashed lines in Fig. 3) and for several other eruptions (e.g., Fig. 2 of Costa et al., 2016). Bimodality can occur due to changes in eruptive intensity, magmatic properties (i.e., composition, crystallinity, vesicularity, and permeability), and/or a large abundance of non-juvenile lithic material (Costa et al., 2016).

## 3.5.2. Total grain-size distribution

Using the Voronoi tessellation method (Bonadonna and Houghton, 2005) with the twenty-five HR-GSDs produces a high-resolution total grain-size distribution (HR-TGSD) for the lower unit of the Cleetwood eruption (Fig. 4) with a median grain-size of  $-2.25~\varphi$  (4.76 mm), and a standard deviation of 2.39  $\varphi$  (0.19 mm). The TGSD exhibits the three distinct modes visible in the individual HD-GSDs: the coarsest population with a median of  $\sim -3~\varphi$  (8 mm), the intermediate mode with a median of  $\sim 0~\varphi$  (1 mm) and the finest population with a median of  $\sim 4.7~\varphi$  (0.04 mm). As discussed in Wiejaczka and Giachetti (2022), given the locations of the 25 samples analyzed, we believe this HR-TGSD is representative of the deposit within 70 km of the vent.

## 3.6. Wind

Filtering the 64,284 wind fields so that only those directed along the main dispersal axis of the lower Cleetwood deposit  $(\pm 2^{\circ})$  are kept leads to a subset of 136 wind fields, corresponding to 0.21% of our original

Table 1
Input parameters and RMSE values for the seven best fits to mass loads and GSD data, respectively.

	Wind	Plume Height (m.a. s.l.)	Alpha	Beta	Mass (kg)	Diffusion Coefficient $(m^2/s)$	Fall time threshold (s)	RMSE ML	RMSE GSD
Best fits to mass loads	2002_10_28_06UTC	18,000	10	6	6.2E+11	5995	2154	56.104	8.646
	2011_10_30_00UTC	18,000	4	1	9E+11	774	1000	56.262	9.077
	2020_03_03_06UTC	15,000	9	1	6.2E + 11	5995	2154	56.282	10.534
	1986_11_30_12UTC	15,000	10	1	9E+11	46,416	1000	56.889	10.693
	1983_12_21_12UTC	15,000	6	1	6.2E + 11	5995	2154	57.058	9.897
	1981_10_25_12UTC	15,000	7	1	6.2E + 11	5995	2154	57.138	10.040
	2021_04_19_06UTC	15,000	10	2	6.2E + 11	2154	10,000	58.144	12.691
Best fits to GSDs	1997_10_26_00UTC	12,000	3	10	6.2E + 11	1,000,000	21,544	226.898	1.396
	1986_11_30_12UTC	12,000	3	10	9E+11	1,000,000	21,544	218.098	1.397
	2015_07_17_00UTC	12,000	3	10	9E+11	1,000,000	46,416	217.693	1.397
	2015_09_07_06UTC	12,000	3	10	3.3E+11	1,000,000	100,000	236.528	1.397
	2011_10_30_00UTC	12,000	3	10	3.3E+11	1,000,000	46,416	236.457	1.397
	1983_12_21_12UTC	12,000	3	10	9E+11	1,000,000	100,000	218.290	1.399
	1981_10_25_12UTC	12,000	2	7	3.3E+11	1,000,000	10,000	235.982	1.400

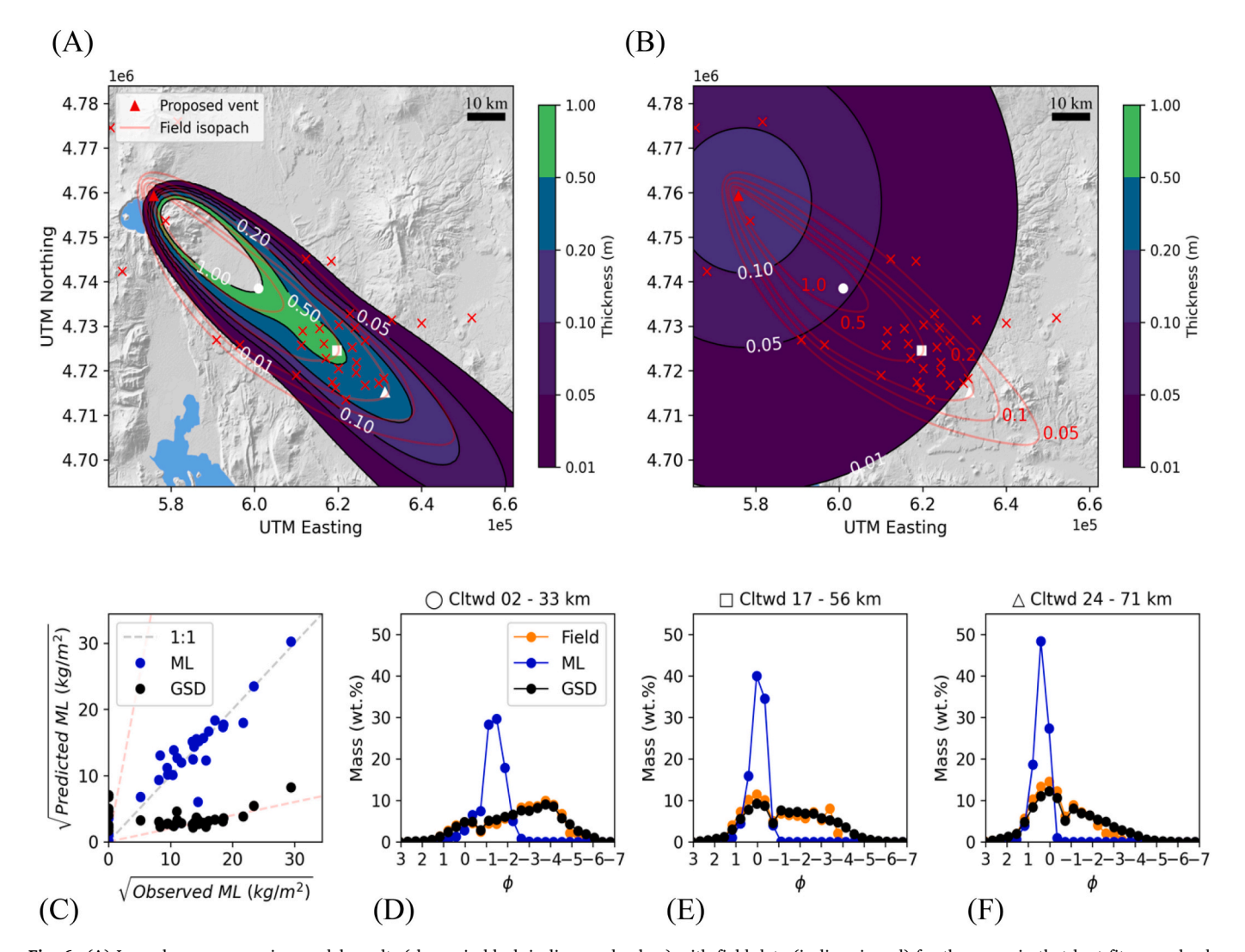


Fig. 6. (A) Isopach map comparing model results (shown in black isolines and colors) with field data (isolines in red) for the scenario that best fits mass loads, obtained with the wind profile measured on 10/28/2006 at 06:00 UTC. Isolines are in meters and are shown for 1 m, 0.5 m, 0.2 m, 0.1 m, and 0.05 m (see labels on B). (B) Isopach map comparing model results with field data for the scenario producing the best fit to grain-size distributions (GSD), obtained with the same wind field. (C) Predicted vs. observed square roots of mass loads for the best fit to mass loads (in blue) and best fit to GSDs (in black). Dashed red lines represent 5 and 1/5 times the 1:1 line. (D—F) Measured and predicted GSDs at three locations along the main dispersal axis. Field data are in orange, scenario for best fit to ML in blue, and best fit to GSD in black. Circle, square and triangle symbols in plot titles correspond to the same symbols on above isopach maps. (For interpretation of the references to colour in this figure legend, the reader is referred to the web version of this article.)

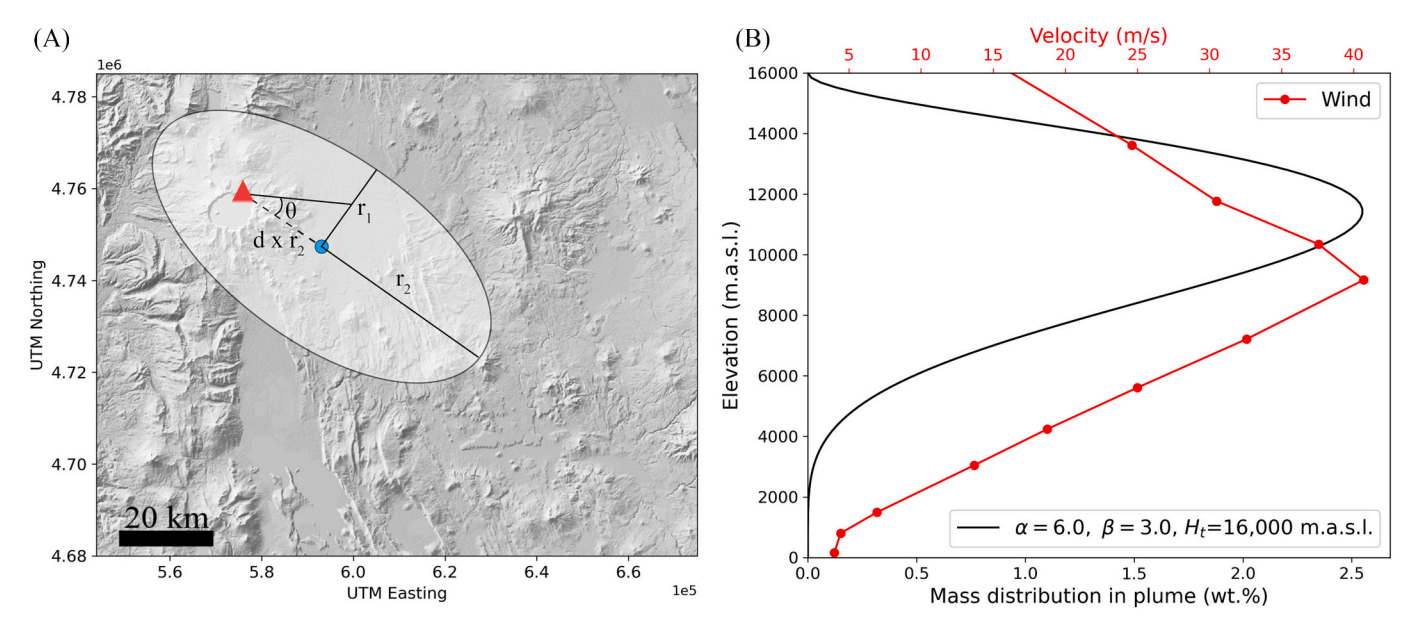


Fig. 7. Schematic showing the parameters controlling the dimensions, location, and orientation of the umbrella cloud laterally (A) and vertically (B). Here  $r_1=20$  km,  $r_2=40$  km,  $\theta=0^{\circ}$ , d=0.15,  $H_t=16$  km,  $\alpha=6$ , and  $\beta=3$ . In B) the beta distribution and wind profile for the best fit umbrella cloud is shown. ~99% of the mass is released above or within the zone of highest wind velocities (i.e., ~5–14 km) illustrating that both the umbrella cloud's geometry and wind contribute to the modeled deposit.

catalog. Most wind fields have their highest velocities at elevations between 7.5 km and 15 km a.s.l., with velocities reaching upwards of 80 m/s at a maximum (Fig. 5). Wind velocity drastically decreases above 16–18 km a.s.l., and at higher altitudes headings move away from the main dispersal axis, usually towards the west. When distributed based on average velocities and time of the year (Supplementary Fig. 3), filtered winds with an average heading of N129°  $\pm$  2° between 2 and 21 km a.s.l. concentrate in the period between September and May. This trend becomes increasingly apparent when only considering wind fields that have average velocities >35 m/s (value obtained from CS86). The Cleetwood eruption thus probably occurred sometime between late summer and mid-spring.

## 3.7. Tephra2 grid search

A total of 9,840,000 scenarios were investigated using Tephra2, corresponding to 41 winds files, 8 values of H<sub>t</sub> (9:3:30 km), 10 values of  $\alpha$  (1:1:10), 10 values of  $\beta$  (1:1:10), 3 values of M (3.3, 6.2, and 9.0  $\times$ 10<sup>11</sup> kg), 10 of DC (log space[2:10:6]) and 10 values of FTT (log space [2:10:5]). The results from a subset of the filtered wind fields are shown in Table 1 and are divided into the parameters that give the lowest RMSE for mass load (top) and the lowest RMSE for grain-size distribution (bottom). Although only a subset, they encapsulate the overall trends observed in all scenarios that are discussed below (for full results of bestfits see Supplementary Table 4). A sensitivity analysis was conducted (Supplementary Fig. 3) to ensure parameters reached a global minimum. Alpha for the best-fit ML is the only scenario in which a global minimum was not reached. For this scenario, we ran more simulations and allowed alpha to increase past 10. We found that the best-fit for ML occurs as  $\alpha$ approaches infinity. In other words, these simulations put all the erupted mass at the top of the plume height. This increase in alpha from 10 to near infinity modestly changes the RMSE ML from 56 to 53, respectively. To comply with common values in the literature, we choose to keep  $\alpha =$ 10 as the maximum.

#### 3.7.1. Best fits to mass loads

For all filtered wind fields, best fitting for mass load (ML) gives plume heights ( $H_t$ ) of 12–30 km a.s.l.,  $\alpha$  and  $\beta$  values of 1–10 and 1–10, respectively, M of (6.2–9.0)  $\times$  10<sup>11</sup> kg, diffusion coefficients (DC) of

 $100-46,416 \,\mathrm{m}^2/\mathrm{s}$ , and fall time thresholds (FTT) of  $1000-100,000 \,\mathrm{s}$ . The lowest RMSE ML of all (56.10) is obtained for the wind field from 10/ 28/2006 at 06:00 UTC with  $\alpha = 10$ ,  $\beta = 6$ ,  $M = 6.2 \times 10^{11}$  kg, DC = 5995 $m^2/s$ , and FTT = 2154 s, which are all consistent with values obtained in previous studies (Bonadonna et al., 2005; Connor and Connor, 2006; Bonadonna et al., 2010; Elissondo et al., 2016) and  $H_t = 18$  km, a value consistent with that obtained by applying the CS86, BC2013, and RS2019 models (9-27 km a.s.l.). Fig. 6c shows that modeled mass loads for this best-case scenario (for ML) are close to the measured ones both near the vent (highest mass loads) and further from it. Modeled isolines are slightly narrower than the field-derived ones, but overall, very close. The parameters that give the lowest RMSE in terms of mass load give a RMSE GSD of 8.65, compared to 1.40 when parameters are optimized to minimize the RMSE GSD (see Section 3.7.2). The same observation is made for all scenarios listed in the upper part of Table 1: parameters optimized to get a low RMSE ML always give a poor fit in terms of GSD, with most of the coarse material being deposited much closer to the vent compared what is seen in the field. Particles  $<-3 \varphi$  (>8 mm) from the coarsest mode do not reach the control points in the corresponding model output GSDs (Fig. 6). This holds true for our closest sample location on the dispersal axis (33 km; Cltwd 2), where particles >8 mm make up 49 wt% of the deposit (Fig. 6D).

## 3.7.2. Grain-size distributions best fits

Best fits for grain-size distributions are obtained with average plume heights of 9–15 km a.s.l.,  $\alpha$  and  $\beta$  of 2–4 and 7–10, respectively, M of  $(3.3–9.0)\times 10^{11}$  kg, high DC of 1000,000 m $^2/s$ , and fall time thresholds (FTT) of 10,000-100,000 s. When the RMSE GSD is minimized, all wind fields give similar RMSE results  $(1.40\pm0.004)$ . The wind field that gives the lowest RMSE GSD is that on 10/26/1997 at 00:00 UTC and lowest RMSE GSD is obtained for  $H_t=12$  km,  $\alpha=3,\,\beta=10,\,M=6.2\times10^{11}$  kg, DC =1000,000 m $^2/s$ , and FTT =21,544 s. For this scenario, the RMSE ML is 226.90 (~4 fold that obtained when parameters are optimized to minimize RMSE ML). When optimizing the GSD, the RMSE ML values are always very high. Isopach maps derived from the best fit RMSE GSD values (Fig. 6) are always much wider and more circular than what is observed in the field, propagating upwind and in all directions around the vent. All the best fits give diffusion coefficients  $(10^6$  m $^2/s)$  up to three orders of magnitude larger than those obtained when best fitting

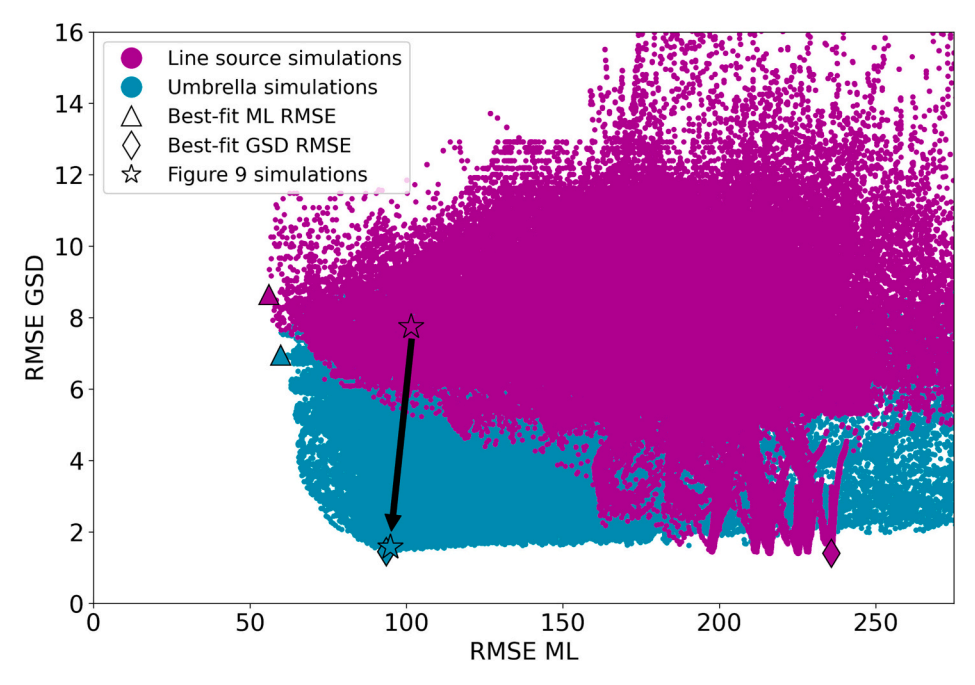


Fig. 8. RMSE ML as a function of RMSE GSD for all simulations using wind field 10/28/2006 06:00 UTC. Note that the addition of an umbrella cloud begins to converge on zero and simultaneously decreases both RMSE ML and GSD over using a single line source. Stars denote the RMSE values for the simulations shown below in Fig. 9.

MLs ( $\sim 10^3 - 10^5 \text{ m}^2/\text{s}$ ) and we discuss below why we believe these DC values are unrealistic. While these are empirical values, diffusion coefficients from eruptions analogous to the Lower Cleetwood are on the same order of magnitude as those obtained here when fitting MLs (e.g., 3900 m²/s for the 2011 eruption of Cordón Caulle; Elissondo et al., 2016), and much lower than those obtained when fitting GSDs. Note that the wind field used in Fig. 6a-b is the same as the one providing the best fit to the mass load data (10/28/2006 at 06:00 UTC).

## 4. Discussion

We use a grid search approach with the Tephra2 VATDM to determine the ESPs that best fit the mass loads and grain-size distributions observed in the field. While the model reproduces well measured MLs *or* GSDs with 'reasonable' ESPs (i.e., consistent with what is found in the literature for eruptions of similar sizes), it fails to give good fits for both MLs *and* GSDs simultaneously (Fig. 6; Table 3).

Past studies have shown that if the lateral spreading of tephra from an umbrella cloud is not accounted for in advection-diffusion models, then both plume height and the diffusion coefficient may be overestimated (Volentik et al., 2010; Magill et al., 2015). Constantinescu et al. (2021) showed that modeling tephra sedimentation using Tephra2 using a disk geometry, rather than a vertical line, gave more reasonable estimations of the ESPs for the 2450 BP eruption of Pululagua (Ecuador), without artificially inflating plume height or the diffusion coefficient. Furthermore, the lateral spreading from umbrella clouds also assists in the transport of coarser particles farther from the vent (Sparks et al., 1992; Sparks et al., 1997; Baines and Sparks, 2005). In our study, both the very high diffusion coefficients required to minimize RMSE GSD and modeled proximal deposits being poor in coarse particles when minimizing RMSE ML suggest that having an umbrella cloud, rather than a single vertical line source, would help improve the fit of the model to the data. Given the pronounced elliptical shape of the lower Cleetwood isopach and the high wind intensity measured kilometers above the vent, it is possible that the lower Cleetwood tephra fall deposit originated from an elliptical umbrella cloud, spreading both upwind and downwind the vent, and elongated roughly in the main direction of wind propagation. Such oval umbrella shapes have been reported at Kelud

 $(100 \times 150 \text{ km}; \text{Kristiansen et al., } 2015)$  and Calbuco  $(50 \times 80 \text{ km}; \text{Romero et al., } 2016; \text{Van Eaton et al., } 2016)$ , for example. To test this hypothesis, we use the output of Tephra2 to calculate what would be the MLs and GSDs if tephra were released from an umbrella cloud, as opposed to from a single vertical line (Fig. 7).

In the original version of Tephra2, the mass is initially released along a single vertical line directly above the vent. The grain size distribution is the same everywhere along this line, and the mass is vertically distributed following parameters  $\alpha$  and  $\beta$ , with the bulk of the mass being concentrated towards the upper part of the plume when  $\alpha > \beta$ (Fig. 2). For a given scenario, dividing the input total mass by X while keeping everything else constant does not change the modeled local GSDs, and give mass loads that are simply divided by X everywhere on the grid. Thus, by dividing the total mass of the original scenario by Xand distributing X identical vertical lines in a disc or oval shape around the vent, one can mimic an umbrella cloud, provided  $\alpha > \beta$  and the mass of the plume is concentrated in its upper section. For such 'umbrella scenario', the total mass load at a given location is then equal to the sum of the X different mass loads at that location obtained from the X different output files. The GSD at that same location is the weighted average of the GSDs of the X different output files, where the weight is the relative contribution, in terms of mass load, of each of the X output files at that location. Although Constantinescu et al., (2021) already modified Tephra2 to mimic tephra release from a disc-shaped umbrella cloud, our approach has the advantage of allowing 1) the use of a custom, non-Gaussian TGSD, 2) elliptically-shaped umbrella cloud geometries, 3) the controlled distribution of the mass vertically in the umbrella cloud by varying  $\alpha$  and  $\beta$ , and 4) the variation of the wind direction and speed with elevation.

We applied this approach using the wind field that produces the best RMSE ML value of all wind files (wind on 10/28/2002 at 06:00 UTC, giving a best RMSE ML of 56.1 with parameters listed in Table 1). We tested whether using an umbrella-shaped cloud can give an even lower best RMSE ML and lower best RMSE GSD than the original line-source scenario, and more importantly, whether it can produce simultaneously low RMSE ML and low RMSE GSD. To do so, we calculated the RMSE ML and RMSE GSD obtained while varying umbrella cloud geometries. We assumed an elliptical umbrella with a semi-minor axis,  $r_1$ , a

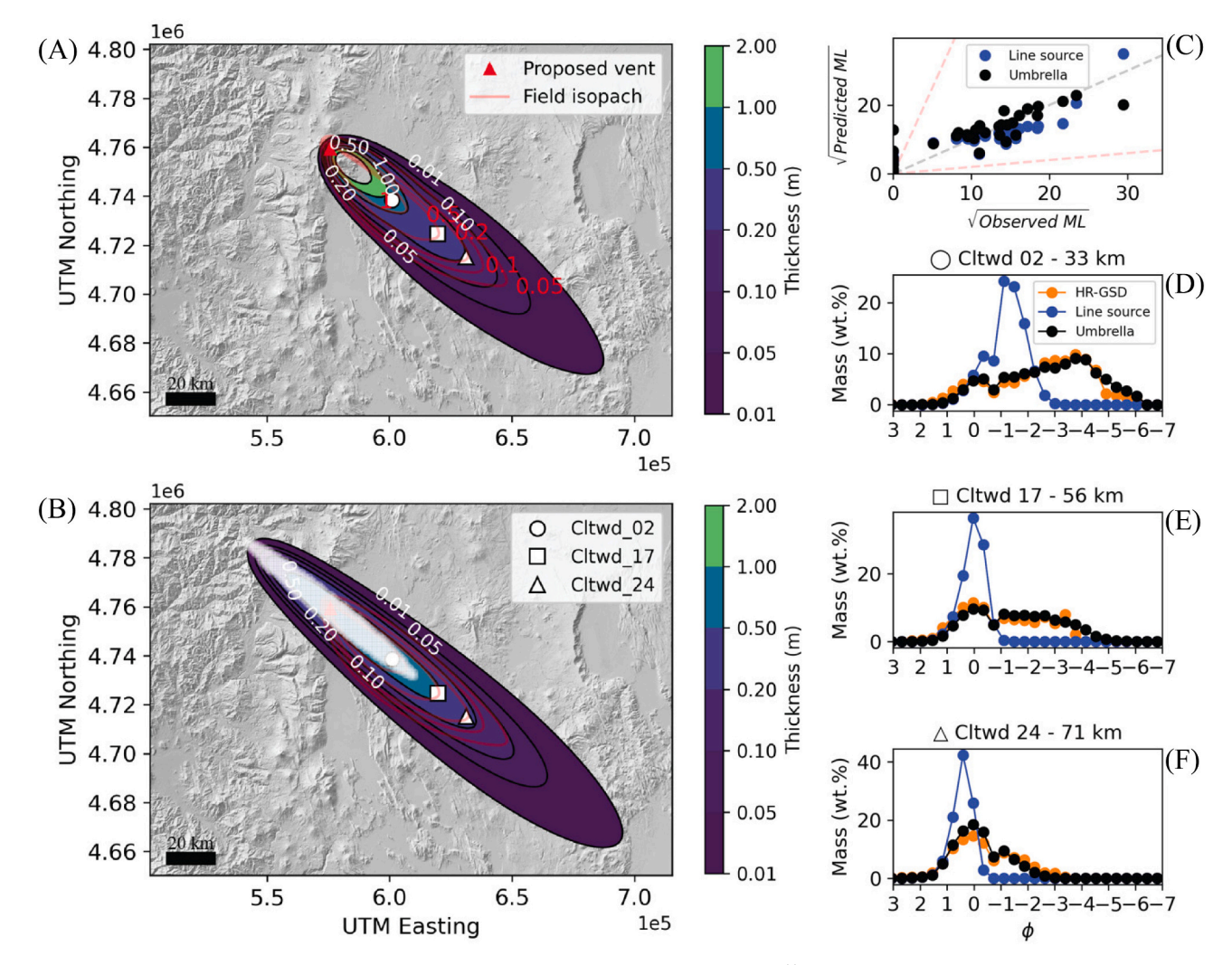


Fig. 9. (A) Isopach map obtained for a line-source scenario with  $H_t=16$  km,  $\alpha=6$ ,  $\beta=3$ ,  $M=6.2\times10^{11}$ , DC=10,000, FTT=4642 and the wind field from 10/28/2006 06:00 UTC. (B) Isopach map obtained using the same parameters but considering tephra release from a  $5\times45$  km $^2$  ( $\theta=0^\circ$ ; d=0) umbrella cloud. White ellipse represents the umbrella cloud geometry used. (C) Predicted vs. observed square root of the mass loads for both the line-source and umbrella cloud scenarios. (D—F) HR-GSDs from line source and umbrella cloud compared with field-derived HR-GSDs. Circle, square, and triangle symbols in plot titles correspond to the same symbols on isopach maps (A-B). All isopachs are in meters and background is global earth relief (Tozer et al., 2019).

semi-major axis,  $r_2$ , and a thickness controlled by plume height and  $\alpha$ and  $\beta$ . We allowed  $r_1$  to vary in the range 1–20 km, and  $r_2$  between 2 and 50 km. We tested plume heights from 14 km to 22 km above sea level every km, the three values of mass used in the line-source scenario, diffusion coefficients between  $10^3$  and  $10^4$  m<sup>2</sup>/s, four values of  $\alpha$  (4, 6, 8, 10), three values of  $\beta$  (1, 2, 3, 6), and a constant FTT = 4642 s. The direction of the umbrella's long axis was allowed to vary by  $\theta$  off the direction of the main dispersal axis of the deposit (N129), with  $-10^{\circ} < \theta < +10^{\circ}$ . We also allowed the oval umbrella to be decentered from the inferred vent by a distance  $d \times r_2$ , keeping the vent located on the long axis of the oval umbrella. We set -1 < d < 1, with d > 0 leading to the umbrella being shifted to the SE compared to the vent and d =0 leading to the vent and umbrella center being superimposed. We first calculated 'line-source' scenarios by varying  $H_t$ ,  $\alpha$ , and DC (with FTT and β constant) and then used the output to calculate a 'umbrella source' scenario by varying r1, r2,  $\theta$ , and d.

After  $\sim\!90~k$  simulations, we find that releasing mass from an umbrella cloud rather than a vertical line significantly improves the fit to mass loads and grain size distributions. Using a plume height of 18 km a. s.l.,  $\alpha=10$ ,  $\beta=6$ , DC =  $6\times10^3~m^2/s$ , FTT = 2154 s,  $r_1=2~km$ ,  $r_2=3~km$ ,  $\theta=1^\circ$ , and d=0.2 gives a RMSE ML of 56.07, which is 0.3% better than the best case using a line-source scenario. Similarly, with a plume

height of 12 km a.s.l.,  $\alpha = 3$ ,  $\beta = 10$ , DC =  $10^4$  m<sup>2</sup>/s, FTT = 21,544 s,  $r_1$  = 6 km,  $r_2 = 14$  km,  $\theta = 3^{\circ}$ , and d = -0.2, the median RMSE GSD decreases to 1.39, which is a 2% better fit than for a release from a vertical line for the same wind file. More importantly, using an umbrella cloud allows to fit both the local mass loads and grain size distributions relatively well simultaneously (Fig. 8), especially improving the fit to GSDs when the fit to mass loads is already good. For example, with a plume height of 16 km a.s.l.,  $\alpha = 6$ ,  $\beta = 3$ ,  $M = 6.2 \times 10^{11}$  kg,  $DC = 10^4$  m<sup>2</sup>/s, FTT = 4642 s, and using an umbrella with characteristics  $r_1 = 5$  km,  $r_2 = 45$  km,  $\theta = 0^{\circ}$ , and d = 0, rather than a vertical line source, leads to an 'improvement' of the RMSE ML by just 1.8%, but greatly improves the median RMSE GSD by 80% (from 42% to 88% locally) compared to a single vertical line source under the same conditions (Fig. 9; Supplementary Table 6). Comparing this umbrella geometry with well observed umbrella clouds show that an elliptical geometry is realistic. For example, the VEI 4 eruption of Kelud (Indonesia) on February 13th, 2014, produced a 200 × 300 km<sup>2</sup> oval shaped umbrella with a radius extending ~40 km upwind and the top of the umbrella region reaching altitudes of 18-19 km a.s.l. (Kristiansen et al., 2015; Goode et al., 2019; Hargie et al., 2019). The best-fit geometries for the lower Cleetwood reflect the minimum size and most concentrated region of the umbrella cloud as this study focuses on the proximal-medial deposit and particles ≥0.125 mm, which

represent ~96 wt% of the modeled mass.

#### 5. Conclusions

The accuracy of Volcanic Ash Transport and Dispersal Models (VATDMs) relies on field studies of analogous eruptions to estimate the initial input Eruption Source Parameters (ESPs). We re-evaluated the ESPs (plume height, erupted mass and TGSD) of the first, main phase of the  $\sim\!7.7$  ka Cleetwood eruption of Mount Mazama (Crater Lake/giiwas, Oregon, United States), the lower Cleetwood unit, which produced  $\sim\!6.2\times10^{11}$  kg of tephra. More than 75% of the twenty-five grain-size distributions measured on the tephra deposit are bimodal, with  $\sim\!96$  wt% of the mass being distributed  $\leq\!3$   $\varphi$  ( $\geq0.125$  mm). Combining a detailed wind analysis with the geometry of the deposit shows that the Cleetwood eruption probably occurred sometime between late summer and mid-spring.

We carried out a grid search approach using the VATDM Tephra2 and the field-derived erupted mass and TGSD to minimize the misfits between the modeled mass loads and high-resolution grain-size distributions and the field-derived ones, at twenty-five locations. The original model, which assumes mass is released vertically along a single line above the vent, reproduces either mass loads or grain-size distributions well, but fails to reproduce both simultaneously. Optimizing the fit for best mass loads results in the coarsest particles falling too close to the vent. On the other hand, minimizing the fit of the model to the fieldderived grain size distributions leads to unrealistically high diffusion coefficients and isopachs. We thus post-treated Tephra2 output to simulate tephra release from an umbrella cloud. Our method allows for the use of a custom TGSD, variable umbrella cloud geometries, vertical mass distribution in the plume, and the use of real 1D wind fields. Grid searching over umbrella cloud geometries and plume heights gives very good results for an elliptical geometry of  $5 \times 45 \text{ km}^2$  reaching 16 km a.s. 1. The addition of this umbrella cloud greatly improves the fits to measured grain size distributions, while maintaining a very good fit to the measured mass loads.

This study demonstrates the value of using high-resolution grain size distributions together with mass loads at individual locations to give insight into the wind conditions and the plume geometry and dimensions of unwitnessed eruptions. Our addition of an umbrella cloud with a custom geometry and mass distribution further emphasizes the importance of considering accurate eruption source parameters to successfully model historic eruptions, especially when the intent of using these results is to mitigate the impacts of future volcanic eruptions. Future improvements would be to allow for variations in the umbrella thickness away from the vent (i.e., by varying  $H_{\rm t}$ ,  $\alpha$ , and  $\beta$  laterally) and allowing for variable GSD both vertically and horizontally within the umbrella, with presumably finer particles towards the upper and distal regions of the umbrella. These improvements, although feasible, would have to be informed by in-situ observations and measurements within volcanic plumes.

#### **Funding**

JW and TG were partly funded by National Science Foundation award 2240044.

#### CRediT authorship contribution statement

**Joshua Wiejaczka:** Writing – review & editing, Writing – original draft, Methodology, Investigation, Formal analysis, Data curation, Conceptualization. **Thomas Giachetti:** Investigation, Funding acquisition, Conceptualization.

## Declaration of competing interest

The authors declare the following financial interests/personal

relationships which may be considered as potential competing interests:

Thomas Giachetti reports financial support was provided by National Science Foundation. If there are other authors, they declare that they have no known competing financial interests or personal relationships that could have appeared to influence the work reported in this paper.

#### Data availability

Data will be made available on request.

#### Acknowledgments

We thank C. McDermott and the University of Oregon's 2023 field camp for their help while working in the Fremont-Winema National Forest. We are grateful to J.M. Watkins, J. Dufek and L.G. Mastin for their valuable feedback. Thanks to A.R. Van Eaton and H.M.N. Wright for their time during laser diffraction analysis at the Cascades Volcano Observatory. We also thank K.V. Cashman, S.R. Young and C.R. Bacon for their insightful discussions about Mount Mazama. We also thank the two anonymous reviewers for their comments which helped improve the manuscript, and to the editors for their efficient handling of the paper.

#### Appendix A. Supplementary data

Supplementary data to this article can be found online at https://doi.org/10.1016/j.jvolgeores.2024.108015.

#### References

Bacon, C.R., 1983. Eruptive history of Mount Mazama and Crater Lake Caldera, Cascade Range, U.S.A. J. Volcanol. Geotherm. Res. 18 (1–4), 57–115. https://doi.org/ 10.1016/0377-0273(83)90004-5.

Baines, P.G., Sparks, R.S.J., 2005. Dynamics of giant volcanic ash clouds from supervolcanic eruptions. Geophys. Res. Lett. 32 (24).

Baxter, P.J., 2005. Human impacts of volcanoes. Volcan. Environ. 273–303.
 Biass, S., Bonadonna, C., Connor, L., Connor, C., 2016. TephraProb: a Matlab package for probabilistic hazard assessments of tephra fallout. J. Appl. Volcanol. 5 (1), 1–16.

Biass, S., Bonadonna, C., Houghton, B.F., 2019. A step-by-step evaluation of empirical methods to quantify eruption source parameters from tephra-fall deposits. J. Appl. Volcanol. 8 (1), 1. https://doi.org/10.1186/s13617-018-0081-1.

Blong, R.J., 1984. Volcanic Hazards: A Sourcebook on the Effects of Eruptions. Elsevier. Blott, S.J., Pye, K., 2006. Particle size distribution analysis of sand-sized particles by laser diffraction: an experimental investigation of instrument sensitivity and the effects of particle shape. Sedimentology 53 (3), 671–685. https://doi.org/10.1111/j.1365-3091.2006.00786.x.

Bonadonna, C., Costa, A., 2013. Plume height, volume, and classification of explosive volcanic eruptions based on the Weibull function. Bull. Volcanol. 75, 742. https://doi.org/10.1007/s00445-013-0742-1.

Bonadonna, C., Houghton, B.F., 2005. Total grain-size distribution and volume of tephrafall deposits. Bull. Volcanol. 67 (5), 441–456. https://doi.org/10.1007/s00445-004-0386-2

Bonadonna, C., Phillips, J.C., 2003. Sedimentation from strong volcanic plumes. J. Geophys. Res. Solid Earth 108 (B7).

Bonadonna, C., Ernst, G.G.J., Sparks, R.S.J., 1998. Thickness variations and volume estimates of tephra fall deposits: the importance of particle Reynolds number. J. Volcanol. Geotherm. Res. 81 (3–4), 173–187.

Bonadonna, C., Connor, C.B., Houghton, B.F., Connor, L., Byrne, M., Laing, A., Hincks, T. K., 2005. Probabilistic modeling of tephra dispersal: Hazard assessment of a multiphase rhyolitic eruption at Tarawera, New Zealand. J. Geophys. Res. Solid Earth 110 (B3). https://doi.org/10.1029/2003JB002896.

Bonadonna, C., Connor, L., Connor, C.B., Courtland, L.M., 2010. Tephra2.

Bonadonna, C., Genco, R., Gouhier, M., Pistolesi, M., Cioni, R., Alfano, F., Ripepe, M., 2011. Tephra sedimentation during the 2010 Eyjafjallajökull eruption (Iceland) from deposit, radar, and satellite observations. J. Geophys. Res. Solid Earth 116 (B12).

Bonadonna, C., Folch, A., Loughlin, S., Puempel, H., 2012. Future developments in modelling and monitoring of volcanic ash clouds: outcomes from the first IAVCEI-WMO workshop on Ash Dispersal Forecast and Civil Aviation. Bull. Volcanol. 74, 1–10.

Brown, R.J., Bonadonna, C., Durant, A.J., 2012. A review of volcanic ash aggregation. Phys. Chem. Earth Parts a/b/c 45, 65–78.

Buckland, H.M., Saxby, J., Roche, M., Meredith, P., Rust, A.C., Cashman, K.V., Engwell, S.L., 2021. Measuring the size of non-spherical particles and the implications for grain size analysis in volcanology. J. Volcanol. Geotherm. Res. 415, 107257 https://doi.org/10.1016/j.jvolgeores.2021.107257.

Carey, S., Sparks, R.S.J., 1986. Quantitative models of the fallout and dispersal of tephra from volcanic eruption columns. Bull. Volcanol. 48 (2), 109–125.

- Castro, J.M., Dingwell, D.B., 2009. Rapid ascent of rhyolitic magma at Chaitén volcano, Chile. Nature 461 (7265), 780–783.
- Connor, L.J., Connor, C.B., 2006. Inversion Is the Key to Dispersion: Understanding Eruption Dynamics by Inverting Tephra Fallout.
- Constantinescu, R., Hopulele-Gligor, A., Connor, C.B., Bonadonna, C., Connor, L.J., Lindsay, J.M., Volentik, A.C., 2021. The radius of the umbrella cloud helps characterize large explosive volcanic eruptions. Commun. Earth Environ. 2 (1), 3.
- Costa, A., Pioli, L., Bonadonna, C., 2016. Assessing tephra total grain-size distribution: Insights from field data analysis. Earth Planet. Sci. Lett. 443, 90–107. https://doi. org/10.1016/j.epsl.2016.02.040.
- Draxler, R.R., Hess, G.D., 1998. An overview of the HYSPLIT\_4 modelling system for trajectories. Aust. Meteorol. Mag. 47 (4), 295–308.
- Elissondo, M., Baumann, V., Bonadonna, C., Pistolesi, M., Cioni, R., Bertagnini, A., Gonzalez, R., 2016. Chronology and impact of the 2011 Cordón Caulle eruption, Chile. Nat. Hazards Earth Syst. Sci. 16 (3), 675–704.
- Folch, A., Mingari, L., Gutierrez, N., Hanzich, M., Macedonio, G., Costa, A., 2020. FALL3D-8.0: a computational model for atmospheric transport and deposition of particles, aerosols and radionuclides–part 1: Model physics and numerics. Geosci. Model Dev. 13 (3), 1431–1458.
- Freret-Lorgeril, V., Donnadieu, F., Eychenne, J., Soriaux, C., Latchimy, T., 2019. In situ terminal settling velocity measurements at Stromboli volcano: Input from physical characterization of ash. J. Volcanol. Geotherm. Res. 374, 62–79.
- Goode, L.R., Handley, H.K., Cronin, S.J., Abdurrachman, M., 2019. Insights into eruption dynamics from the 2014 pyroclastic deposits of Kelut volcano, Java, Indonesia, and implications for future hazards. J. Volcanol. Geotherm. Res. 382, 6–23.
- Gouhier, M., Donnadieu, F., 2008. Mass estimations of ejecta from Strombolian explosions by inversion of Doppler radar measurements. J. Geophys. Res. Solid Earth 113 (R10)
- Hargie, K.A., Van Eaton, A.R., Mastin, L.G., Holzworth, R.H., Ewert, J.W., Pavolonis, M., 2019. Globally detected volcanic lightning and umbrella dynamics during the 2014 eruption of Kelud, Indonesia. J. Volcanol. Geotherm. Res. 382, 81–91.
- Heiken, G., 1978. Plinian-type eruptions in the medicine lake highland, California, and the nature of the underlying magma. J. Volcanol. Geotherm. Res. 4 (3), 375–402. https://doi.org/10.1016/0377-0273(78)90023-9.
- Johnston, E.N., Phillips, J.C., Bonadonna, C., Watson, I.M., 2012. Reconstructing the tephra dispersal pattern from the Bronze Age eruption of Santorini using an advection-diffusion model. Bull. Volcanol. 74, 1485–1507.
- Jones, A., Thomson, D., Hort, M., Devenish, B., 2007. In: Borrego, C., Norman, A.-L. (Eds.), The U.K. Met Office's Next-Generation Atmospheric Dispersion Model, NAME III BT - Air Pollution Modeling and its Application XVII. Springer US, Boston, MA.
- Kanamitsu, M., Ebisuzaki, W., Woollen, J., Yang, S.-K., Hnilo, J.J., Fiorino, M., Potter, G. L., 2002. NCEP–DOE AMIP-II Reanalysis (R-2). Bull. Am. Meteorol. Soc. 83 (11), 1631–1644. https://doi.org/10.1175/BAMS-83-11-1631.
- Kozono, T., Iguchi, M., Miwa, T., Maki, M., Maesaka, T., Miki, D., 2019. Characteristics of tephra fall from eruptions at Sakurajima volcano, revealed by optical disdrometer measurements. Bull. Volcanol. 81, 1–18.
- Kristiansen, N.I., Prata, A.J., Stohl, A., Carn, S.A., 2015. Stratospheric volcanic ash emissions from the 13 February 2014 Kelut eruption. Geophys. Res. Lett. 42 (2), 588–596.
- Kuehn, S.C., 2002. Stratigraphy, Distribution, and Geochemistry of the Newberry Volcano Tephras. Washington State University.
- Magill, C., Mannen, K., Connor, L., Bonadonna, C., Connor, C., 2015. Simulating a multiphase tephra fall event: inversion modelling for the 1707 Hoei eruption of Mount Fuji, Japan. Bull. Volcanol. 77, 1–18.
- Pioli, L., Bonadonna, C., Pistolesi, M., 2019. Reliability of Total Grain-size distribution of Tephra Deposits. Sci. Rep. 9 (1), 1–15. https://doi.org/10.1038/s41598-019-46125-8.

- Pistolesi, M., Cioni, R., Bonadonna, C., Elissondo, M., Baumann, V., Bertagnini, A., Francalanci, L., 2015. Complex dynamics of small-moderate volcanic events: the example of the 2011 rhyolitic Cordón Caulle eruption, Chile. Bull. Volcanol. 77 (1), 1–24.
- Romero, J.E., Morgavi, D., Arzilli, F., Daga, R., Caselli, A., Reckziegel, F., Perugini, D., 2016. Eruption dynamics of the 22–23 April 2015 Calbuco Volcano (Southern Chile): analyses of tephra fall deposits. J. Volcanol. Geotherm. Res. 317, 15–29.
- Rose, W.I., Durant, A.J., 2011. Fate of volcanic ash: Aggregation and fallout. Geology 39 (9), 895-896.
- Rossi, E., Bonadonna, C., Degruyter, W., 2019. A new strategy for the estimation of plume height from clast dispersal in various atmospheric and eruptive conditions. Earth Planet. Sci. Lett. 505, 1–12. https://doi.org/10.1016/j.epsl.2018.10.007.
- Schindelin, J., Arganda-Carreras, I., Frise, E., Kaynig, V., Longair, M., Pietzsch, T., Cardona, A., 2012. Fiji: an open-source platform for biological-image analysis. Nat. Methods 9 (7), 676–682. https://doi.org/10.1038/nmeth.2019.
- Schipper, C.I., Castro, J.M., Tuffen, H., James, M.R., How, P., 2013. Shallow vent architecture during hybrid explosive–effusive activity at Cordón Caulle (Chile, 2011–12): evidence from direct observations and pyroclast textures. J. Volcanol. Geotherm. Res. 262, 25–37.
- Schwaiger, H.F., Denlinger, R.P., Mastin, L.G., 2012. Ash3d: A finite-volume, conservative numerical model for ash transport and tephra deposition. J. Geophys. Res. Solid Earth 117 (B4). https://doi.org/10.1029/2011JB008968.
- Scollo, S., Coltelli, M., Prodi, F., Folegani, M., Natali, S., 2005. Terminal settling velocity measurements of volcanic ash during the 2002–2003 Etna eruption by an X-band microwave rain gauge disdrometer. Geophys. Res. Lett. 32 (10).
- Searcy, C., Dean, K., Stringer, W., 1998. PUFF: a high-resolution volcanic ash tracking model. J. Volcanol. Geotherm. Res. 80 (1–2), 1–16.
- Sparks, R.S.J., Bursik, M.I., Ablay, G.J., Thomas, R.M.E., Carey, S.N., 1992.
  Sedimentation of tephra by volcanic plumes. Part 2: controls on thickness and grain-size variations of tephra fall deposits. Bull. Volcanol. 54, 685–695.
- Sparks, R.S.J., Bursik, M.I., Carey, S.N., Gilbert, J., Glaze, L.S., Sigurdsson, H., Woods, A. W., 1997. Volcanic plumes. Wiley.
- Suzuki, T., 1983. A theoretical model for dispersion of tephra. Arc Volcan. 95, 113. Trafton, K.R., Giachetti, T., 2021. The morphology and texture of Plinian pyroclasts reflect their lateral sourcing in the conduit. Earth and Planet. Sci. Lett. 562, 116844.
- Trafton, K.R., Giachetti, T., 2022. The pivotal role of Vulcanian activity in ending the explosive phase of rhyolitic eruptions: the case of the big Obsidian Flow eruption (Newberry Volcano, USA). Bull. Volcanol. 84 (12), 104.
- Van Eaton, A.R., Amigo, Á., Bertin, D., Mastin, L.G., Giacosa, R.E., González, J., Behnke, S.A., 2016. Volcanic lightning and plume behavior reveal evolving hazards during the April 2015 eruption of Calbuco volcano, Chile. Geophys. Res. Lett. 43 (7), 3563–3571.
- Volentik, A.C.M., Connor, C.B., Connor, L.J., Bonadonna, C., 2009. Aspects of volcanic hazard assessment for the Bataan nuclear power plant, Luzon Peninsula, Philippines. In: Volcanic and Tectonic Hazard Assessment for Nuclear Facilities, pp. 229–256.
- Volentik, A.C., Bonadonna, C., Connor, C.B., Connor, L.J., Rosi, M., 2010. Modeling tephra dispersal in absence of wind: Insights from the climactic phase of the 2450 BP Plinian eruption of Pululagua volcano (Ecuador). J. Volcanol. Geotherm. Res. 193 (1–2), 117–136.
- Wiejaczka, J., Giachetti, T., 2022. Using eruption source parameters and high-resolution grain-size distributions of the 7.7 ka Cleetwood Eruption of Mount Mazama (Oregon, United States) to reveal primary and secondary eruptive processes. Front. Earth Sci. 460
- Wilson, T.M., Stewart, C., Sword-Daniels, V., Leonard, G.S., Johnston, D.M., Cole, J.W., Barnard, S.T., 2012. Volcanic ash impacts on critical infrastructure. Phys. Chem. Earth Parts a/b/c 45, 5–23.